

## Dominance of $\gamma$ - $\gamma$ electron-positron pair creation in a plasma driven by high-intensity lasers

Yutong He<sup>1</sup>, Thomas G. Blackburn<sup>2</sup>, Toma Toncian<sup>3</sup> & Alexey V. Arefiev<sup>1</sup>✉

Creation of electrons and positrons from light alone is a basic prediction of quantum electrodynamics, but yet to be observed. Our simulations show that the required conditions are achievable using a high-intensity two-beam laser facility and an advanced target design. Dual laser irradiation of a structured target produces high-density  $\gamma$  rays that then create  $>10^8$  positrons at intensities of  $2 \times 10^{22} \text{ Wcm}^{-2}$ . The unique feature of this setup is that the pair creation is primarily driven by the linear Breit-Wheeler process ( $\gamma\gamma \rightarrow e^+e^-$ ), which dominates over the nonlinear Breit-Wheeler and Bethe-Heitler processes. The favorable scaling with laser intensity of the linear process prompts reconsideration of its neglect in simulation studies and also permits positron jet formation at experimentally feasible intensities. Simulations show that the positrons, confined by a quasistatic plasma magnetic field, may be accelerated by the lasers to energies  $>200$  MeV.

<sup>1</sup>University of California at San Diego, La Jolla, CA, USA. <sup>2</sup>Department of Physics, University of Gothenburg, Gothenburg, Sweden. <sup>3</sup>Institute for Radiation Physics, Helmholtz-Zentrum Dresden-Rossendorf e.V., Dresden, Germany. ✉email: [aarefiev@eng.ucsd.edu](mailto:aarefiev@eng.ucsd.edu)

High-power lasers, focused close to the diffraction limit, create ultrastrong electromagnetic fields that can be harnessed to drive high fluxes of energetic particles and to study fundamental physical phenomena<sup>1</sup>. At intensities exceeding  $10^{23} \text{ W cm}^{-2}$ , those energetic particles can drive nonlinear quantum-electrodynamical (QED) processes<sup>2,3</sup> otherwise only found in extreme astrophysical environments<sup>4,5</sup>. One such process is the creation of electron-positron pairs from light alone. Whereas multiphoton (nonlinear) pair creation has been measured once, using an intense laser<sup>6</sup>, the two-photon process ( $\gamma\gamma \rightarrow e^+e^-$ , referred to here as the linear Breit–Wheeler process<sup>7</sup>) has yet to be observed in the laboratory with real photons. As the probability of the nonlinear process grows nonperturbatively with increasing field strength<sup>8,9</sup>, it is expected to provide the dominant contribution to pair cascades in high-field environments, including laser–matter interactions beyond the current intensity frontier<sup>10,11</sup> and pulsar magnetospheres<sup>12</sup>.

The small size of the linear Breit–Wheeler cross section means that high photon flux is necessary for its observation. Achieving the necessary flux requires specialized experimental configurations<sup>13,14</sup> and therefore its possible contribution to in situ electron–positron pair creation has hitherto been neglected in studies of high-intensity laser–matter interactions. However, these interactions create not only regions of ultrastrong electromagnetic field, but also high fluxes of accelerated particles, because relativistic effects mean that even a solid-density target can become transparent to intense laser light<sup>15,16</sup>. In the situation of multiple colliding laser pulses, which is the most advantageous geometry for driving nonlinear QED cascades<sup>10,17–19</sup>, there are, as a consequence, dense, counterpropagating flashes of  $\gamma$  rays, and so the neglect of linear pair creation may not be appropriate.

Recent construction of multi-beam high-intensity laser facilities, such as Extreme Light Infrastructure Beamlines<sup>20</sup>, Extreme Light Infrastructure Nuclear Physics (ELI-NP)<sup>21,22</sup>, and Apollon<sup>23</sup>, and a significant progress in fabrication of  $\mu\text{m}$ -scale structured targets<sup>24,25</sup> open up qualitatively novel regimes of pair production for exploration. Specifically, we show that a structured plasma target irradiated by two laser beams creates an environment where the linear process dominates over the nonlinear and over the Bethe–Heitler process. Remarkably, this regime does not require laser intensities beyond than what is currently available. At  $I_0 < 5 \times 10^{22} \text{ W cm}^{-2}$ , the positron yield from the linear process is  $\sim 10^9$ , which is four orders of magnitude greater than that envisaged by Pike et al.<sup>13</sup> and Ribeyre et al.<sup>14</sup> These positrons are generated when two high-energy electron beams, accelerated by and copropagating with laser pulses that are guided along a plasma channel, collide head-on, emitting synchrotron photons that collide with each other and the respective oncoming laser. Not only does this provide an opportunity to study the linear Breit–Wheeler process itself, which is of interest because of its role in astrophysics<sup>26–28</sup>, but also the transition between linear and nonlinear-dominated pair cascades. In an astrophysical context, the balance between these two determines how a pulsar magnetosphere is filled with plasma; as in the laser–plasma scenario, the controlling factors are the field strength and photon flux<sup>29–32</sup>. We also show that the positrons, created inside the plasma channel coterminously with the laser pulses, may be confined and accelerated to energies of hundreds of MeV, which raises the possibility of generating positron jets. The transverse confinement needed to accelerate positrons is provided by a slowly evolving plasma magnetic field. Crucially, it is the same field that enables acceleration of the ultra-relativistic electrons prior to the collision of the two laser pulses.

An overview of the key results of this paper is shown in Fig. 1: we show that a structured target, when irradiated from both sides by intense laser pulses, enables the creation of a large yield of

positrons through  $\gamma$ - $\gamma$  collisions, i.e., the linear Breit–Wheeler process, at intensities well within the reach of existing high-power laser facilities. Two beams of electrons, accelerated along the plasma channel [Fig. 1a], collide with the respective counter-propagating laser [Fig. 1b], and emit  $\gamma$  rays that themselves collide to produce electron–positron pairs [Fig. 1c]. Furthermore, we show that a quasistatic magnetic field, created by the propagation of the lasers through the plasma channel [Fig. 1c], is sustained over sufficiently long times, and with the correct topology, to enable confinement and acceleration of the positrons, rather than electrons, so generated [Fig. 1d, e].

## Results

The target configuration considered in this work is shown in Fig. 1a. A structured plastic target with a prefilled channel is irradiated from both sides by two 50 fs, high-intensity laser pulses that have the same peak normalized laser amplitude  $a_0$ , in the range  $100 \leq a_0 \leq 190$ . Here  $a_0 = 0.85 I_0^{1/2} [10^{18} \text{ W cm}^{-2}] \lambda_0 [\mu\text{m}]$ , where  $I_0$  is the peak intensity of the laser and  $\lambda_0 = 1 \mu\text{m}$  its wavelength in vacuum. The target structure, where a channel of width  $d_{\text{ch}} = 5 \mu\text{m}$  and electron density  $n_e = (a_0/100)3.8n_c$  is embedded in a bulk with higher density  $n_e = 100n_c$ , enables stable propagation<sup>33</sup> and alignment of the two lasers. Here  $n_c = \pi m c^2 / (e \lambda_0)^2$  is the so-called critical density, where  $e$  is the elementary charge,  $m$  is the electron mass, and  $c$  is the speed of light. At relativistic laser intensities ( $a_0 \gg 1$ ), the cutoff density for the laser increases roughly linearly with  $a_0$  due to relativistically induced transparency. Scaling the channel density with  $a_0$  ensures that the optical properties of the channel and thus the phase velocity of the laser wave-fronts are approximately unchanged with increase of  $a_0$ . Structured targets with empty channels have successfully been used in experiments<sup>24,25</sup> and it is now possible to fabricate targets with prefilled channels, similar to those considered in this work<sup>34</sup>.

The interaction is simulated in 2D-3V with the fully relativistic particle-in-cell (PIC) code EPOCH<sup>35</sup>, which includes Monte Carlo modules for quantum synchrotron radiation and nonlinear pair creation<sup>36</sup>. At each time-step, the quantum synchrotron radiation module computes the quantum nonlinearity parameter,

$$\chi \equiv \frac{\gamma}{E_s} \sqrt{\left( \mathbf{E} + \frac{1}{c} [\mathbf{v} \times \mathbf{B}] \right)^2 - \frac{1}{c^2} (\mathbf{E} \cdot \mathbf{v})^2}, \quad (1)$$

for each charged macro-particle using the electric and magnetic fields ( $\mathbf{E}$  and  $\mathbf{B}$ ) at the particle location, as well as the particle relativistic factor  $\gamma$  and velocity  $\mathbf{v}$ . Here  $E_s \approx 1.3 \times 10^{18} \text{ V/m}$  is the Schwinger field<sup>37–39</sup>. The parameter  $\chi$  controls the total radiation power and the energy spectrum of the emitted photons. In the quantum regime  $\chi \gtrsim 1$ , which is reached in this work, it is necessary to take into account the recoil experienced by the particle when emitting individual photons. This is done self-consistently by the PIC simulation, which uses the Monte Carlo algorithm described by Ridgers et al.<sup>36</sup> and Gonoskov et al.<sup>40</sup> Note that, since the ion species is fully ionized carbon, Bethe–Heitler pair creation, already demonstrated in laser-driven experiments<sup>41,42</sup>, may be neglected. Detailed simulation and target parameters are provided in the Methods section. All the results presented in this paper have been appropriately normalized by taking the size of the ignored dimension to be equal to the channel width  $d_{\text{ch}}$ , i.e.,  $5 \mu\text{m}$ .

**Electron acceleration.** The plasma channel, being relativistically transparent to the intense laser light<sup>15,16</sup>, acts as an optical waveguide. The laser pulses propagate with nearly constant transverse size through the channel, pushing plasma electrons forward. This longitudinal current generates a slowly evolving,

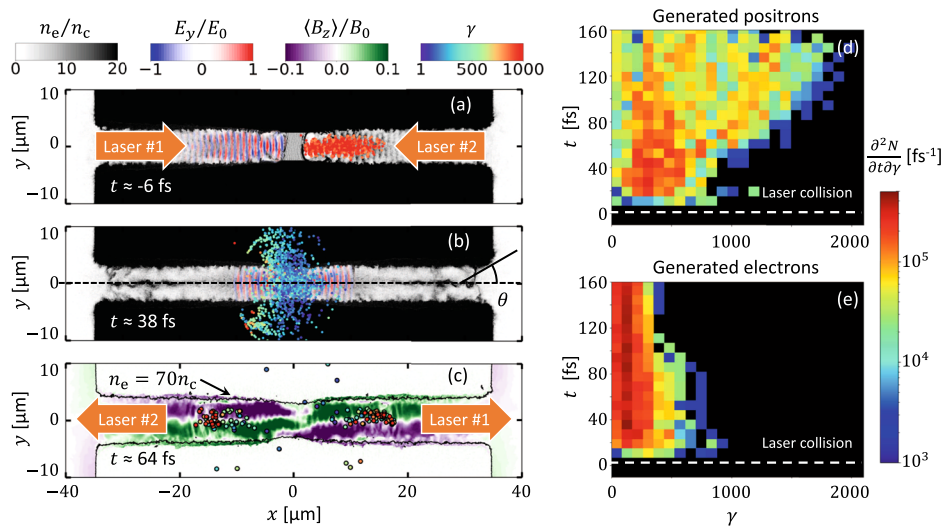


**Fig. 1 Positron production and acceleration in a structured plasma target.** Results from a 2D-3V particle-in-cell (PIC) simulation of two laser pulses with  $a_0 = 190$  irradiating a structured plasma target. **a** Electron density  $n_e$  (gray scale), transverse electric field of laser #1  $E_y$  (color scale) and energetic electrons with  $\gamma \geq 800$  accelerated by laser #2 (dots, colored by  $\gamma$ ). **b** Total transverse electric field  $E_y$  (color scale) and electrons from panel **(a)**. **c** Laser-accelerated positrons (points), confined by the quasistatic plasma magnetic field ( $B_z$ ) (color scale).  $E_0$  and  $B_0$  are the peak laser electric and magnetic fields in vacuum. Time evolution of the energy spectra of **d** positrons and **e** electrons generated by nonlinear Breit-Wheeler pair creation: the horizontal, dashed lines indicates the time at which the lasers collide.

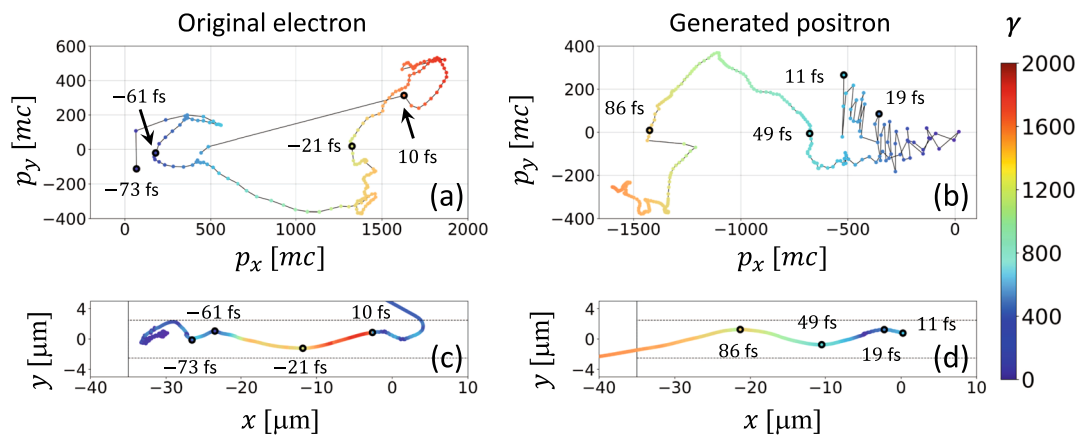


**Fig. 2 Trajectories of an accelerated plasma electron and a generated positron.** Trajectories of an accelerated plasma electron and a generated positron from the 2D PIC simulation shown in Fig. 1: **a, b** transverse momenta  $p_x$ ,  $p_y$  and **c, d** position in the  $x$ - $y$  plane. Color coding denotes the magnitude of the relativistic factor  $\gamma$ . The vertical solid line is the initial position of the left edge of the target. The horizontal dashed lines show the initial location of the channel walls. The timestep between the colored markers is 0.5 fs. Timestamps are provided for selected markers (shown as dark circles) to facilitate comparison between trajectories in  $(p_x, p_y)$ -space and  $(x, y)$ -space. To improve visibility, the electron trajectory in **(a)** is shown for  $-73 \text{ fs} \leq t \leq 11 \text{ fs}$ .

azimuthal magnetic field with peak magnitude 0.6 MT (30% of the laser magnetic field strength) at  $a_0 = 190$ , as shown in Fig. 1c. The magnetic field enables confinement and direct laser acceleration of the electrons<sup>33,43</sup>. After propagating for  $\sim 30 \mu\text{m}$  along the channel, laser #2 in Fig. 1a has accelerated a left-moving, high-energy, high-charge electron beam that performs transverse oscillations of amplitude  $\sim 2 \mu\text{m}$ : the number of electrons with relativistic factor  $\gamma > 800$  is  $4 \times 10^{11}$ , which is equivalent to a charge of 64 nC. Laser #1 generates a similar population of electrons moving to the right, with a representative electron trajectory shown in Fig. 2a, c.

The plasma magnetic field has an essential role in enabling generation of ultrarelativistic electrons. Transverse deflections by the magnetic field keep  $p_y$  antiparallel to the transverse electric field  $E_y$  of the laser, despite the oscillation of the latter. As a result, the electron continues to gain energy while moving along the channel and performing transverse oscillations, as may be seen in

Fig. 2a, c. In the absence of the magnetic field, the oscillations of  $E_y$  would terminate the energy gain prematurely. The magnetic field of the plasma has to be sufficiently strong to ensure that the electron deflections occur on the same time scale as the oscillations of  $E_y$ . This criterion can be formulated in terms of the longitudinal plasma current<sup>43</sup>. Note that the same confinement and acceleration would occur for a positron, if the positron were moving in the opposite direction along the  $x$ -axis, as its charge has opposite sign. This is shown in Fig. 2b, d and discussed in more detail in Positron acceleration. The evolution of the energy of the electron population as a whole is shown in Fig. 3, where we see the bulk of the electrons reach energies of several hundreds of MeV.

**Radiation emission.** The target length is such that no appreciable depletion of the laser pulses occurs by the time they reach the midplane ( $x = 0$ ),  $t = 0$ . Here, the high-energy electron beams

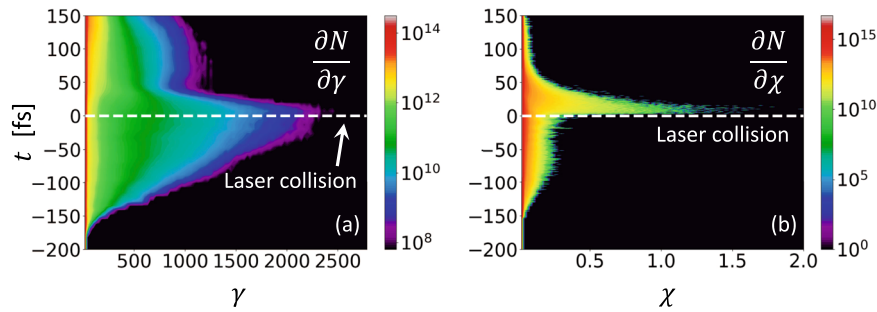


**Fig. 3 Growth and collapse of the electron  $\gamma$  and  $\chi$  as the laser collision occurs.** Time evolution of the distributions of the **a** electron relativistic factor  $\gamma$  and **b** quantum nonlinearity parameter  $\chi$ , defined by Eq. (1), for the 2D PIC simulation shown in Fig. 1. The two laser pulses have  $a_0 = 190$  and collide at  $t = 0$ , which is shown by the horizontal dashed lines.

collide head-on with the respective oncoming laser pulse, each of which has an intensity at least as large as its initial value (the magnitude can increase slightly due to pulse shaping during propagation along the channel). This configuration maximizes the quantum nonlinearity parameter  $\chi$  for the electrons, as the two terms under the square root in Eq. (1) are additive for counterpropagation. (In copropagation, by contrast, they almost cancel each other, which is why radiation prior to the collision, when electrons propagate in the same direction as the accelerating laser pulse, is driven primarily by the plasma magnetic field.) Figure 3a, as well as Fig. 1b, shows the impact of the collision on the energetic electrons from Fig. 1a: they radiate away a substantial fraction of the energy they gained during the acceleration phase and are scattered out of the channel. Similar behavior is shown in Fig. 2c: the electron encounters the counterpropagating laser beam at about  $t = 10$  fs and then its energy decreases rapidly. As is shown in Fig. 3b,  $\chi \lesssim 0.25$  before the collision occurs; immediately thereafter, the cancellation is eliminated,  $\chi$  increases rapidly to  $\sim 1.25$ , and then it collapses due to the radiative energy loss.

The configuration under consideration here therefore represents a micron-scale, plasma-based realization of an all-optical laser–electron-beam collision<sup>17</sup>. This geometry is the subject of theoretical<sup>44–46</sup> and experimental<sup>47,48</sup> investigation into radiative energy loss in the quantum regime, as well as nonlinear pair creation<sup>49</sup>. It is worth emphasizing that the use of the structured target has two key benefits compared to the commonly used gas targets: automatic alignment of the colliding electrons with an oncoming laser beam and a considerably higher density of colliding electrons.

The observed increase in  $\chi$  during the electron–laser collision increases the radiation power of the individual electrons. The conversion efficiency of the laser energy into photons with energies  $100 \text{ keV} \leq \epsilon_\gamma \leq 10 \text{ MeV}$  is shown in Fig. 4a over a wide range of  $a_0$ . We are interested in the photons in this energy range because these are the photons that participate in the linear Breit–Wheeler process in our setup (see Methods). As expected, there is a significant increase in the conversion rate caused by the electron–laser collision. The angularly resolved spectrum of the emitted photons is shown in Fig. 4b. There are  $\sim 2 \times 10^{14}$  photons with energies between 100 keV and 10 MeV and with  $90^\circ \leq \theta \leq 180^\circ$ . This is essentially half of the energetic photons emitted by the left-moving electrons (the other half is emitted with  $-180^\circ \leq \theta \leq -90^\circ$  and has a similar spectrum). Furthermore, this emission occurs in a highly localized region, which leads to the marked increase in photon density shown in Fig. 4c, d for the case where  $a_0 = 190$ .

**Positron acceleration.** The photons emitted by one electron beam collide with both the oncoming laser and the photons emitted by the other electron beam. The former drives

electron–positron pair creation by the nonlinear Breit–Wheeler process,  $\gamma \xrightarrow{\text{EM field}} e^+ e^-$ <sup>2,9</sup>: at  $a_0 = 190$ , our simulations predict a yield of  $5 \times 10^8$  pairs.

The positrons subsequently undergo direct laser acceleration in much the way as the electrons: PIC simulations show that the typical relativistic factor of a right-moving positron increases to  $\gamma \approx 1000$  as it propagates from  $x \approx 0$  to  $x \approx 20 \mu\text{m}$ . This is illustrated in Fig. 1c and corroborated by the time evolution of the positron energy spectrum shown in Fig. 1d. A representative trajectory for a positron moving from the central region towards the left target boundary is shown in Fig. 2d. Acceleration is made possible by the plasma magnetic field, which is confining (on the left-hand side of the target) for electrons moving to the right, or equivalently, positrons moving to the left [compare Fig. 2c, d]. Crucially, Fig. 1c shows that this magnetic field polarity is preserved well after the lasers and electron beams collide. This is why, after the two laser pulses collide and pass through each other, they can accelerate the positrons, but not the electrons, created in by photon–photon collisions, as seen in Fig. 1e. The generated electrons are not transversely confined in our magnetic field configuration when moving from the center towards either of the channel openings. However, the continued propagation of the lasers along the channel raises the possibility of accelerating positron jets, if there is sufficient pair creation in the channel center.

**Competing positron generation mechanisms.** We now show that there is prolific pair creation in the channel center, and furthermore that it is dominated by the linear Breit–Wheeler process. The cross section is<sup>7</sup>:

$$\sigma_{\gamma\gamma} = \frac{\pi r_e^2}{2\zeta} \left[ (3 - \beta^4) \ln \left( \frac{1 + \beta}{1 - \beta} \right) - 2\beta(2 - \beta^2) \right], \quad (2)$$

where  $r_e = e^2/(mc^2)$  is the classical electron radius,  $\beta = \sqrt{1 - 1/\zeta}$ , and  $\sqrt{\zeta}$  is the normalized center-of-mass energy,  $\zeta = \epsilon_1 \epsilon_2 (1 - \cos \psi)/(2m^2 c^4)$ , for two photons with energy  $\epsilon_{1,2}$  colliding at angle  $\psi$ . Equation (2) is the cross section for two-photon pair creation in vacuum: while it is modified by a strong electromagnetic field<sup>50–53</sup>, these corrections, which scale as  $(\chi_\gamma/\zeta)^2$  for photon quantum nonlinearity parameter  $\chi_\gamma$ <sup>54</sup>, are negligible for the scenario under consideration here (see Supplementary Note 3 for details).

We take as a representative value  $\sigma_{\gamma\gamma} \approx 2r_e^2$  (approximately its maximum, at  $\zeta \approx 2$ ) and assume that we have two photon populations of number density  $n_\gamma$ , colliding head-on in a volume of length  $c\tau$  (the laser pulse length) and width  $d_{\text{ch}}$  (the width of the channel). The number of photons (in each beam) is  $N_\gamma \approx 10^9 \lambda_0 [\mu\text{m}] P_\gamma (n_e/n_c) (c\tau/\lambda_0) (d_{\text{ch}}/\lambda_0)^2$ , where  $P_\gamma$  is the

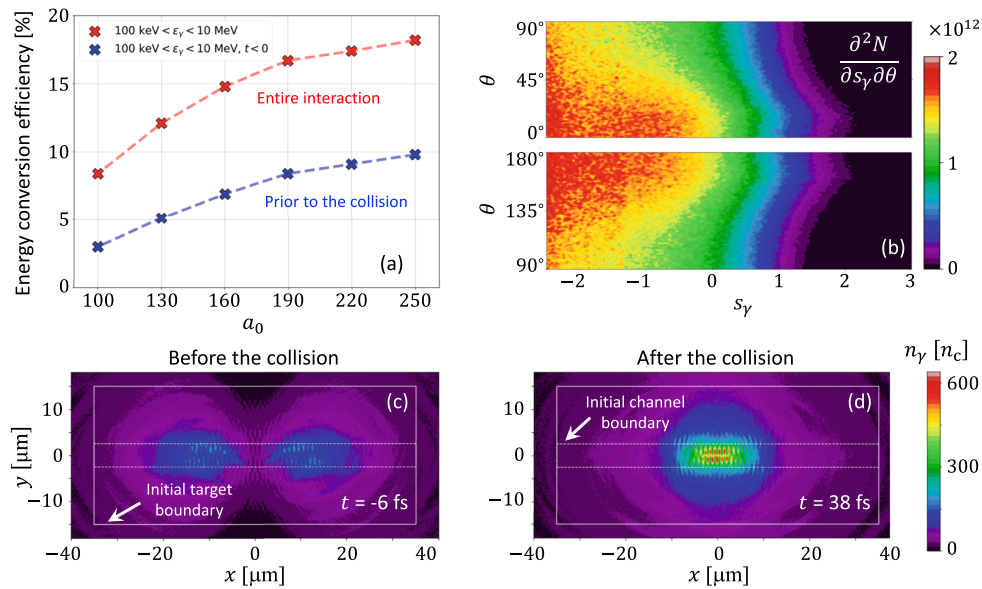


**Fig. 4 MeV photon emission inside the structured target.** Results from the 2D PIC simulation shown in Fig. 1, where the two counterpropagating lasers have  $a_0 = 190$ . **a** Conversion efficiency of the laser energy into  $\gamma$  rays with energies  $100 \text{ keV} \leq \epsilon_\gamma \leq 10 \text{ MeV}$ : (blue markers) before the two lasers collide at  $x = 0$  and (red markers) over the whole laser-target interaction. **b** Energy-angle spectrum,  $\frac{\partial^2 N}{\partial s_\gamma \partial \theta}$  [ $^{\circ-1}$ ], of the photons emitted inside the channel. Here  $\theta$  is the angle defined in Fig. 1b and  $s_\gamma \equiv \log_{10}(\epsilon_\gamma [\text{MeV}])$ . (The spectrum for  $-180^\circ \leq \theta \leq 0^\circ$  is similar). **c, d** The density of photons with energy  $\epsilon_\gamma \geq 1 \text{ keV}$ , in units of the critical density  $n_c$ , before and after the laser-laser collision.

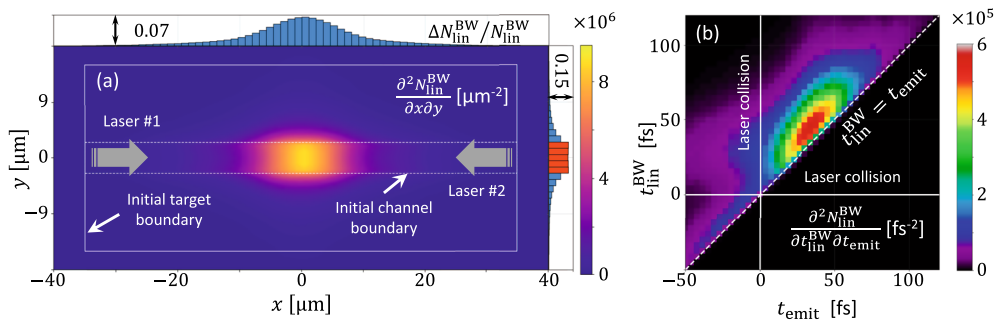


**Fig. 5 Distribution of linear Breit-Wheeler pairs upon their creation.** **a** Probability density that an electron-positron pair is created by the linear Breit-Wheeler process at longitudinal and transverse coordinate  $x$  and  $y$ . The density integrated over  $x$  ( $y$ ), and normalized to the total number of pairs, is shown to the right (above). **b** Probability density that an electron-positron pair is created by the linear Breit-Wheeler process at time  $t_{\text{lin}}^{\text{BW}}$ , by photons that were emitted at times  $t_{\text{emit}}$ . The density includes a normalizing factor of  $1/2$  because each pair has two parent photons. Both plots are obtained by post-processing the 2D PIC simulation from Fig. 1, where the lasers have  $a_0 = 190$ , using the algorithm described in Methods. An equivalent for the nonlinear process is given in Supplementary Note 2.

number of photons emitted per electron,  $n_e$  is the electron number density and  $\lambda_0$  is the laser wavelength. The number of positrons produced,  $N_{\text{lin}}^{\text{BW}} = 2N_\gamma \sigma_{\gamma\gamma} / d_{\text{ch}}^2$ , follows as  $N_{\text{lin}}^{\text{BW}} \approx 40P_\gamma^2 (n_e/n_c)^2 (c\tau/\lambda_0)^2 (d_{\text{ch}}/\lambda_0)^2$ . The physical parameters are  $n_e = 7n_c$ ,  $\tau = 50 \text{ fs}$ ,  $d_{\text{ch}} = 5 \mu\text{m}$ , and  $\lambda_0 = 1 \mu\text{m}$ . The number of photons emitted per laser period by a counterpropagating electron is  $P_\gamma \approx 18\alpha a_0$ , where  $\alpha \approx 1/137$  is the fine-structure constant. By setting  $P_\gamma = 20$ , we obtain a total number of photons,  $2N_\gamma \approx 1.3 \times 10^{14}$ , which is approximately consistent with the simulation result. As a consequence, we predict that  $N_{\text{lin}}^{\text{BW}} \approx 7 \times 10^9$ . Given that  $P_\gamma \propto a_0$  and  $n_e \propto a_0$ , we predict a scaling of  $N_{\text{lin}}^{\text{BW}} \propto a_0^4$ .

This is considerably larger than the number of pairs expected from the nonlinear Breit-Wheeler process; moreover, as the probability rate for the latter is exponentially suppressed with decreasing  $a_0$ , we expect the yield to be much more sensitive to

reductions in laser intensity. The potential dominance of the linear process motivates a precise computation, which takes into account the energy, angle, and temporal dependence of the photon emission.

However, direct implementation of the linear Breit-Wheeler process in a PIC code is a significant computational challenge, as it involves binary collisions of macroparticles and the interaction must be simulated in at least 2D. The simulation at  $a_0 = 190$  generates  $\sim 10^8$  macroparticles in the energy range relevant for linear Breit-Wheeler pair creation and therefore  $\sim 10^{16}$  possible pairings. This can be reduced by using bounding volume hierarchies<sup>55</sup>, which is effective if the photon emission and the pair creation are well-separated in time and space. In our case, there is no such separation. As such, we postprocess the simulation output to obtain the yield of linear Breit-Wheeler pairs, using the algorithm described in Methods. Note that the photons used to compute this yield are the same photons used by

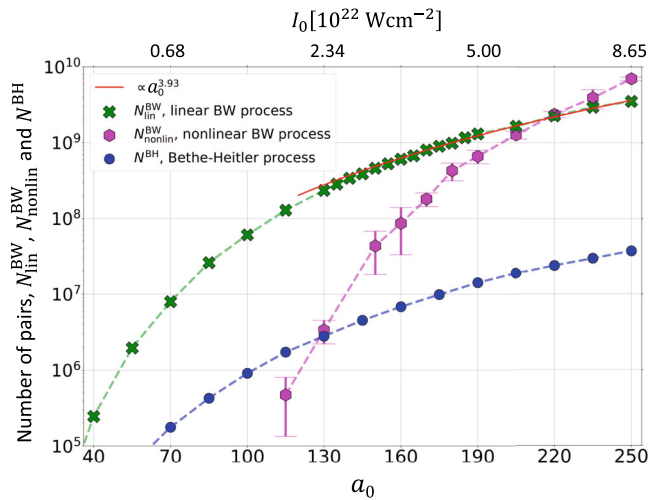


**Fig. 6 Number of electron-positron pairs created by the three most important mechanisms.** The number of electron-positron pairs created by the linear,  $N_{\text{lin}}^{\text{BW}}$ , and nonlinear,  $N_{\text{nonlin}}^{\text{BW}}$ , Breit-Wheeler processes (green crosses and magenta markers, respectively), for the setup shown in Fig. 1, at given normalized laser amplitude  $a_0$  (and equivalent peak intensity  $I_0$ ). Error bars on the nonlinear results indicate statistical uncertainties (at one standard deviation): see text for details. The estimated background, electron-positron pairs produced by the Bethe-Heitler process,  $N^{\text{BH}}$ , is shown by blue circles. The nonlinear Breit-Wheeler pair yield is calculated directly by the PIC code, whereas the linear Breit-Wheeler and Bethe-Heitler pair yields are obtained by post-processing, as described in Methods.

the simulation to compute the yield of nonlinear Breit-Wheeler pairs. As such, while the photon number would change if the simulation were performed in 3D rather than 2D, the yield of both processes would be affected in a similar way.

**Positron yield.** The location and time that pairs are created by the linear process, as determined by this algorithm for the case that  $a_0 = 190$ , are shown in Fig. 5a, b respectively. Approximately 59% of the pairs are created inside the original channel boundary. The majority (74%) of pairs are created by photons emitted after  $t = 0$ , when the high-energy electrons collide with the respective counterpropagating laser. There is a smaller contribution from photons that are emitted during the acceleration phase,  $t_{\text{emit}} < 0$ ; radiation in this case is driven by the plasma magnetic field, because the energetic electrons are moving in the same direction as the laser<sup>33,56</sup>. The dominance of the post-collision contribution is caused by the increase in the quantum parameter  $\chi$  for counterpropagation. The fact the pair creation overlaps with the laser pulses (in both time and space) indicates that the positrons could be accelerated out of the channel, as the magnetic field, shown in Fig. 1c, has the correct orientation to confine them.

The pair yields for the linear and nonlinear processes are compared in Fig. 6. The results for the latter are obtained by performing four simulation runs for each value of  $a_0$  with different random seeds: points and error bars give the mean and standard deviation obtained, respectively. At  $a_0 < 145$ , fewer than ten macropositrons are generated per run, so the corresponding data points are not shown. Our analytical estimates for linear Breit-Wheeler pair creation lead us to expect a yield that scales as  $a_0^4$ ; this is consistent with a power-law fit to the data in Fig. 6, which gives a scaling  $\propto a_0^m$ , where  $m \approx 3.93$ . We find that the linear pair yield is significantly larger for  $a_0 < 190$ .

The number of positrons produced by the linear Breit-Wheeler process exceeds  $10^6$  even for  $a_0 = 50$ , equivalent to

$I_0 = 3.4 \times 10^{21} \text{ W cm}^{-2}$ , which is well in reach of today's high-power laser facilities. In order to determine whether this is sufficient to be observed, we estimate the number of pairs produced by the Bethe-Heitler process, which is the principal source of background. In this process, a  $\gamma$  ray with energy  $\hbar\omega > 2mc^2$  creates an electron-positron pair by interacting with the Coulomb field of an atomic nucleus. The calculation is described in detail in the Methods section. We sum the pair creation probabilities for each simulated photon, taking into account the distance each photon travels in the plasma channel, to obtain the blue circles in Fig. 6. The Bethe-Heitler background is smaller than the linear Breit-Wheeler signal by approximately two orders of magnitude, which supports the feasibility of using a plasma channel as a platform for investigating fundamental QED effects.

## Discussion

We have shown that laser-plasma interactions provide a platform to generate and accelerate positrons, created entirely by light and light, at intensities that are within the reach of current high-power laser facilities. While previous research into pair creation at high intensity has focused largely on the nonlinear Breit-Wheeler process, we show that the high density of photons afforded by a laser-plasma interaction can make the linear process dominant instead. As such, the geometry we consider has the potential to enable the first experimental measurement of two-photon pair creation, driven entirely by real photons. More broadly, it motivates reconsideration of the neglect of two-particle interactions in simulations of dense, laser-irradiated plasmas. Such interactions will form a major component of the physics investigated in upcoming high-power laser facilities. From the theory perspective, our results also motivate investigation of field-driven corrections to the two-photon cross section. The theory for the inverse process, pair annihilation to two photons, has recently been revisited<sup>57</sup>.

One of our surprising findings, besides the dominance of the linear Breit-Wheeler process, is that the plasma magnetic field preserves its polarity after the two laser pulses collide and pass through each other. The polarity of the magnetic field enables transverse confinement of the positrons within the channel and their acceleration by one of the laser pulses to energies approaching 1 GeV. We have confirmed this directly for the positrons generated via the nonlinear Breit-Wheeler process. This should also be the case for the positrons generated via the dominant linear Breit-Wheeler process, because the particles are created inside the channel magnetic field in the presence of a laser pulse, which are the prerequisites for the direct laser acceleration. We therefore expect the positrons to be ejected from the target in the form of collimated jets. The collimation should aid positron detection outside of the target. Moreover, their detection at lower values of  $a_0$  should be a clear indicator of the linear Breit-Wheeler process being the source, as the nonlinear process is heavily suppressed for  $a_0 \lesssim 150$ .

Finally, we point out that our observations regarding the dominance of the linear Breit-Wheeler process apply to a range of channel densities. In our simulations, the electron density in the channel is set at  $n_{\text{ch}} = (a_0/100)3.8n_c$ , such that it increases linearly with  $a_0$  during the intensity scan. Two channel density scans provided in Supplementary Note 1 show that our observations hold for channel densities that are within a  $\pm 20\%$  window of  $n_{\text{ch}}$ .

## Methods

**Particle-in-cell simulations.** Table 1 provides detailed parameters for the simulations presented in the manuscript. Simulations were carried out using the fully relativistic PIC code EPOCH<sup>35</sup>. All our simulations are 2D-3V.

**Table 1 2D PIC simulation parameters.**

Laser parameters		
Normalized field amplitude	$a_0 = 100\text{--}190$	
Peak intensity range	$I_0 = 1.4\text{--}4.9 \times 10^{22} \text{ W/cm}^2$	
Wavelength	$\lambda_0 = 1 \mu\text{m}$	
Focal plane of laser #1	$x = -35 \mu\text{m}$	
Focal plane of laser #2	$x = +35 \mu\text{m}$	
Laser profile (longitudinal and transverse)	Gaussian	
Pulse duration (full width at half maximum for intensity)	50 fs	
Focal spot size (full width at half maximum for intensity)	3.6 $\mu\text{m}$	
Target parameters		
Target thickness (along $y$ )	30 $\mu\text{m}$	
Target length (along $x$ )	70 $\mu\text{m}$	
Channel width	$d_{\text{ch}} = 5 \mu\text{m}$	
Composition	$\text{C}^{+6}$ and electrons	
Channel density	$n_e = 3.8\text{--}7.1n_c$	
Bulk density	$n_e = 100n_c$	
Other parameters		
Simulation box	80 $\mu\text{m}$ in $x$ ; 36 $\mu\text{m}$ in $y$	
Spatial resolution	40 cells per $\mu\text{m}$ in $x$ 20 cells per $\mu\text{m}$ in $y$	
Macro-particles per cell	40 for electrons 20 for carbon ions	

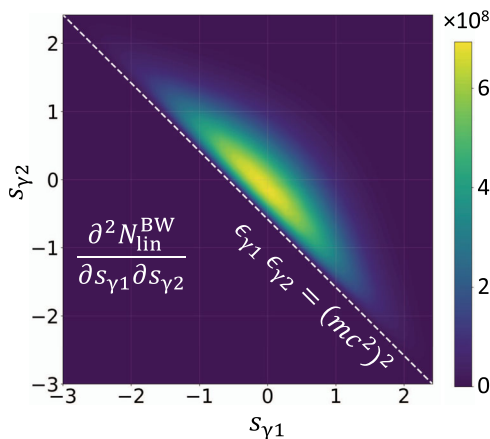


**Fig. 7 Yield of the linear Breit-Wheeler process as a function of photon energies.** Distribution of linear Breit-Wheeler pairs as a function of photon energies for colliding laser pulses with  $a_0 = 190$ .

The axis of the structured target is aligned with the axis of the counterpropagating lasers (laser #1 and laser #2) at  $y = 0$ . The target is initialized as a fully-ionized plasma with carbon ions. The bulk electron density is constant during the intensity scan while the electron density in the channel is set at  $n_e = (a_0/100)3.8n_c$ . Each laser is focused at the corresponding channel opening. The lasers are linearly polarized with the electric field being in the plane of the simulation. In the absence of the target, the lasers have the same Gaussian profile in the focal spot with the same Gaussian temporal profile.

We performed additional runs at  $a_0 = 190$  with higher spatial resolutions (40 by 40 cells per  $\mu\text{m}$  and 80 by 80 cells per  $\mu\text{m}$ ). There are no significant variations in the photon spectra for multi-MeV photons and for photons with energies above 50 keV. The electrons that emit energetic photons, as the one whose trajectories in physical and momentum space are shown in Fig. 2a, c, undergo their energy gain without alternating deceleration to nonrelativistic energies and re-acceleration. This is likely the reason why they are not subject to a more severe constraint<sup>58–60</sup> that requires for the cell-size/time-step to be reduced according to the  $1/a_0$  scaling in order to achieve convergence.

**Postprocessing algorithm for determination of the linear Breit-Wheeler pair yield.** In order to compute the yield and spatial distribution of the linear Breit-Wheeler pairs, we approximate the photon population as a collection of

collimated, monoenergetic beamlets. Discretization into beamlets is achieved by recording the location  $(x_0, y_0)$ , energy  $\epsilon_\gamma$ , and angle  $\theta$  of each photon macroparticle at the time of the emission  $t_{\text{emit}}$ . The photon emission pattern suggests that the emission profile across the channel can be approximated as uniform. We thus represent the emitted photons by a time-dependent distribution function  $f = f(x_0, s_\gamma, \theta, t_{\text{emit}})$ , where  $s_\gamma \equiv \log_{10}(\epsilon_\gamma/\text{MeV})$ . It is sufficient to limit our analysis to  $-40 \mu\text{m} \leq x_0 \leq 40 \mu\text{m}$ ,  $-3 \leq s_\gamma < 3$ , and  $0^\circ \leq \theta \leq 180^\circ$ . We split each interval into 70 equal segments to obtain  $2.6 \times 10^5$  beamlets. We only check for collisions of beamlets propagating to the right with beamlets propagating to the left. The yield is multiplied by a factor of two to account for beamlets with  $-180^\circ \leq \theta \leq 0^\circ$ .

The temporal dependence of a beamlet is represented by slices of given density and fixed thickness. For each beamlet pairing, our algorithm finds the interaction volume  $V$ , the intersections of the beamlet axes and the crossing angle  $\psi$ . The pair yield is given by  $\Delta N_{\text{lin}}^{\text{BW}} = \sigma_{\gamma\gamma} c(1 - \cos \psi) V \int n_1 n_2 dt$ , where  $n_1$  and  $n_2$  are the photon densities in two overlapping slices at the intersection point. In general, the shape of the overlapping region is not rectangular, so the pair creation is visualized by depositing  $\Delta N_{\text{lin}}^{\text{BW}}$  onto a rectangular grid, into cells with centers inside volume  $V$ . The procedure is repeated for each beamlet pairing to obtain the density of generated pairs.

To show that the limitation  $-3 \leq s_\gamma < 3$  is justified, we plot the distribution of linear Breit-Wheeler pairs as a function of photon energies. We use  $s_\gamma$  rather than  $\epsilon_\gamma$  to capture a wide range of energies. Figure 7 confirms that the pair yield drops off for  $|s_\gamma| > 2$ , which justifies the energy range selected in the manuscript.

The algorithm is a simplification that replaces a direct approach of evaluating all possible collisions of beamlet slices. In a head-on collision, each slice collides with many counterpropagating slices within the interaction volume, which makes the calculation computationally intensive. Our algorithm takes advantage of the fact that the typical duration of beamlet emission,  $\tau$ , is much longer than the time it takes for photons to travel between the sources emitting the two beamlets,  $\ell/c$ , where  $\ell$  is the distance between the sources in the case of near head-on collision. As shown in Supplementary Note 4, our approach is a good approximation as long as  $\ell/c\tau < 1$ , with the error scaling as  $(\ell/c\tau)^2$ .

The postprocessing algorithm neglects the depletion of the photon population due to the linear Breit-Wheeler process. This is justifiable, because only a small fraction of the considered photons actually pair-create (and would therefore be lost). Using the maximum photon density of  $n_\gamma \approx 600n_c$  from Fig. 4, we obtain a mean free path with respect to the linear Breit-Wheeler process,

$$1/\sigma_{\gamma\gamma}n_\gamma \approx 6 \times 10^4 \mu\text{m}, \quad (3)$$

that is much larger than the characteristic size of the photon cloud of  $10 \mu\text{m}$ . We estimate depletion of the photon population due to the linear Breit-Wheeler process (as a fraction of the initial size) to be smaller than  $2 \times 10^{-4}$ .

**Estimated background from Bethe-Heitler pair creation.** The principal source of background in a prospective measurement of linear (or nonlinear) Breit-Wheeler pair creation is the Bethe-Heitler process, wherein a photon with energy  $\hbar\omega > 2mc^2$  produces an electron-positron pair on collision with an atomic nucleus<sup>61</sup>. In order to estimate the contribution from this process, we sum the pair creation probability for each macroparticle in the simulation:  $N_{\text{BH}} = \sum_k w_k P_{k,\text{BH}}$ , where  $w_k$  is the weight of the  $k$ th photon, scaled assuming that the third dimension has size  $5 \mu\text{m}$ . The probability  $P_{k,\text{BH}} = n_i \ell_k \sigma_{\text{BH}}$ , where  $n_i$  is the density of carbon ions in the channel and  $\ell_k$  is the distance the photon travels before it leaves the channel. We estimate  $n_i$  and  $\ell_k$  using the unperturbed properties of the channel, i.e., those at the start of the simulation, and taking into account the photon's point of emission and direction of propagation. Thus  $n_i = 3.8a_0 n_c / (100Z)$ . We approximate the cross section  $\sigma_{\text{BH}}$  by that for an unscreened, fully ionized, point carbon nucleus (formula 3D-0000 given by Motz et al.<sup>62</sup> with  $Z = 6$ ). The functional dependence of the cross section on the normalized photon energy  $\gamma = \hbar\omega/(mc^2)$  is given by  $\sigma_{\text{BH}}(\gamma) \simeq \alpha r_e^2 Z^2 (2\pi/3)[(\gamma - 2)/\gamma]^3$  for  $\gamma - 2 \ll 1$  and  $\sigma_{\text{BH}}(\gamma) \simeq \alpha r_e^2 Z^2 [28 \ln(2\gamma)/9 - 218/27]$  for  $\gamma \gg 1$ , where  $r_e$  is the classical electron radius<sup>62</sup>. Our results are shown as blue circles in Fig. 6. This estimate neglects contributions from pair creation in the plasma bulk, which can be controlled by reducing the thickness of the channel walls. Furthermore, the difference in magnitude between background and signal is sufficiently large that it provides a margin of safety.

### Data availability

The datasets generated during and/or analyzed during the current study are available from the corresponding author on reasonable request.

### Code availability

PIC simulations were performed with the open-source, open-access PIC code EPOCH<sup>35</sup>. The photon-photon collision code is based on the algorithm detailed in the Methods and Section 4 of the Supplementary Note 4. It is available from the corresponding author on reasonable request.

Received: 9 March 2021; Accepted: 24 May 2021;

Published online: 17 June 2021

## References

- Zhang, P., Bulanov, S. S., Seipt, D., Arefiev, A. V. & Thomas, A. G. R. Relativistic plasma physics in supercritical fields. *Phys. Plasmas* **27**, 050601 (2020).
- Erber, T. High-energy electromagnetic conversion processes in intense magnetic fields. *Rev. Mod. Phys.* **38**, 626–659 (1966).
- Di Piazza, A., Müller, C., Hatsagortsyan, K. Z. & Keitel, C. H. Extremely high-intensity laser interactions with fundamental quantum systems. *Rev. Mod. Phys.* **84**, 1177–1228 (2012).
- Harding, A. K. & Lai, D. Physics of strongly magnetized neutron stars. *Rep. Prog. Phys.* **69**, 2631–2708 (2006).
- Ruffini, R., Vereshchagin, G. & Xue, S.-S. Electron-positron pairs in physics and astrophysics: from heavy nuclei to black holes. *Phys. Rep.* **487**, 1–40 (2010).
- Burke, D. L. et al. Positron production in multiphoton light-by-light scattering. *Phys. Rev. Lett.* **79**, 1626–1629 (1997).
- Breit, G. & Wheeler, J. A. Collision of two light quanta. *Phys. Rev.* **46**, 1087–1091 (1934).
- Reiss, H. R. Absorption of light by light. *J. Math. Phys.* **3**, 59–67 (1962).
- Ritus, V. I. Quantum effects of the interaction of elementary particles with an intense electromagnetic field. *J. Sov. Laser Res.* **6**, 497–617 (1985).
- Bell, A. R. & Kirk, J. G. Possibility of prolific pair production with high-power lasers. *Phys. Rev. Lett.* **101**, 200403 (2008).
- Ridgers, C. P. et al. Dense electron-positron plasmas and ultraintense  $\gamma$  rays from laser-irradiated solids. *Phys. Rev. Lett.* **108**, 165006 (2012).
- Timokhin, A. N. & Harding, A. K. On the maximum pair multiplicity of pulsar cascades. *Astrophys. J.* **871**, 12 (2019).
- Pike, O., Mackenroth, F., G., H. E. & Rose, S. J. A photon-photon collider in a vacuum hohlraum. *Nat. Photon.* **8**, 434–436 (2014).
- Ribeyre, X. et al. Pair creation in collision of  $\gamma$ -ray beams produced with high-intensity lasers. *Phys. Rev. E* **93**, 013201 (2016).
- Kaw, P. & Dawson, J. Relativistic nonlinear propagation of laser beams in cold overdense plasmas. *Phys. Fluids* **13**, 472–481 (1970).
- Palaniyappan, S. et al. Dynamics of relativistic transparency and optical shuttering in expanding overdense plasmas. *Nat. Phys.* **8**, 763–769 (2012).
- Zhu, X.-L. et al. Dense GeV electron-positron pairs generated by lasers in near-critical-density plasmas. *Nat. Commun.* **7**, 13686 (2016).
- Grismayer, T., Vranic, M., Martins, J. L., Fonseca, R. A. & Silva, L. O. Seeded QED cascades in counterpropagating laser pulses. *Phys. Rev. E* **95**, 023210 (2017).
- Gonoskov, A. et al. Ultrabright GeV photon source via controlled electromagnetic cascades in laser-dipole waves. *Phys. Rev. X* **7**, 041003 (2017).
- Weber, S. et al. P3: an installation for high-energy density plasma physics and ultra-high intensity laser-matter interaction at ELI-Beamlines. *Matter Radiat. at Extremes* **2**, 149–176 (2017).
- Gales, S. et al. The extreme light infrastructure–nuclear physics (ELI-NP) facility: new horizons in physics with 10 PW ultra-intense lasers and 20 MeV brilliant gamma beams. *Rep. Prog. Phys.* **81**, 094301 (2018).
- Lureau, F. et al. High-energy hybrid femtosecond laser system demonstrating  $2 \times 10$  pw capability. *High Power Laser Sci. Eng.* **8**, e43 (2020).
- Papadopoulos, D. et al. The Apollon 10 PW laser: experimental and theoretical investigation of the temporal characteristics. *High Power Laser Sci. Eng.* **4**, e34 (2016).
- Snyder, J. et al. Relativistic laser driven electron accelerator using micro-channel plasma targets. *Phys. Plasmas* **26**, 033110 (2019).
- Bailly-Grandvaux, M. et al. Ion acceleration from microstructured targets irradiated by high-intensity picosecond laser pulses. *Phys. Rev. E* **102**, 021201 (2020).
- Gould, R. J. & Schröder, G. Opacity of the universe to high-energy photons. *Phys. Rev. Lett.* **16**, 252–254 (1966).
- Bonometto, S. & Rees, M. J. On possible observable effects of electron pair production in QSOs. *Mon. Not. R. Astron. Soc.* **152**, 21–35 (1971).
- Piran, T. The physics of gamma-ray bursts. *Rev. Mod. Phys.* **76**, 1143–1210 (2005).
- Burns, M. L. & Harding, A. K. Pair production rates in mildly relativistic magnetized plasmas. *Astrophys. J.* **285**, 747–757 (1984).
- Zhang, B. & Qiao, G. J. Two-photon annihilation in the pair formation cascades in pulsar polar caps. *Astron. Astrophys.* **338**, 62–68 (1998).
- Voisin, G., Mottez, F. & Bonazzola, S. Electron-positron pair production by gamma-rays in an anisotropic flux of soft photons, and application to pulsar polar caps. *Mon. Not. R. Astron. Soc.* **474**, 1436–1452 (2017).
- Chen, A. Y., Cruz, F. & Spitkovsky, A. Filling the magnetospheres of weak pulsars. *Astrophys. J.* **889**, 69 (2020).
- Stark, D. J., Toncian, T. & Arefiev, A. V. Enhanced multi-MeV photon emission by a laser-driven electron beam in a self-generated magnetic field. *Phys. Rev. Lett.* **116**, 185003 (2016).
- Williams, J. Private communications at General Atomics (2019).
- Arber, T. D. et al. Contemporary particle-in-cell approach to laser-plasma modelling. *Plasma Phys. Control. Fusion* **57**, 113001 (2015).
- Ridgers, C. P. et al. Modelling gamma-ray photon emission and pair production in high-intensity laser-matter interactions. *J. Comp. Phys.* **260**, 273–285 (2014).
- Sauter, F. Über das Verhalten eines Elektrons im homogenen elektrischen Feld nach der relativistischen Theorie Diracs. *Z. Phys.* **69**, 742 (1931).
- Heisenberg, W. & Euler, H. Folgerungen aus der Diracschen Theorie des Positrons. *Z. Phys.* **98**, 714 (1936).
- Schwinger, J. On gauge invariance and vacuum polarization. *Phys. Rev.* **82**, 664–679 (1951).
- Gonoskov, A. et al. Extended particle-in-cell schemes for physics in ultrastrong laser fields: review and developments. *Phys. Rev. E* **92**, 023305 (2015).
- Chen, H. et al. Relativistic positron creation using ultraintense short pulse lasers. *Phys. Rev. Lett.* **102**, 105001 (2009).
- Sarri, G. et al. Table-top laser-based source of femtosecond, collimated, ultrarelativistic positron beams. *Phys. Rev. Lett.* **110**, 255002 (2013).
- Gong, Z. et al. Direct laser acceleration of electrons assisted by strong laser-driven azimuthal plasma magnetic fields. *Phys. Rev. E* **102**, 013206 (2020).
- Neitz, N. & Di Piazza, A. Stochasticity effects in quantum radiation reaction. *Phys. Rev. Lett.* **111**, 054802 (2013).
- Blackburn, T. G., Ridgers, C. P., Kirk, J. G. & Bell, A. R. Quantum radiation reaction in laser–electron-beam collisions. *Phys. Rev. Lett.* **112**, 015001 (2014).
- Vranic, M., Grismayer, T., Fonseca, R. A. & Silva, L. O. Quantum radiation reaction in head-on laser-electron beam interaction. *New J. Phys.* **18**, 073035 (2016).
- Cole, J. M. et al. Experimental evidence of radiation reaction in the collision of a high-intensity laser pulse with a laser-wakefield accelerated electron beam. *Phys. Rev. X* **8**, 011020 (2018).
- Poder, K. et al. Experimental signatures of the quantum nature of radiation reaction in the field of an ultraintense laser. *Phys. Rev. X* **8**, 031004 (2018).
- Lobet, M., Davoine, X., d’Humières, E. & Gremillet, L. Generation of high-energy electron-positron pairs in the collision of a laser-accelerated electron beam with a multipetawatt laser. *Phys. Rev. Accel. Beams* **20**, 043401 (2017).
- Ng, Y. J. & Tsai, W. Pair creation by photon-photon scattering in a strong magnetic field. *Phys. Rev. D* **16**, 286–294 (1977).
- Kozlenkov, A. A. & Mitrofanov, I. G. Two-photon production of  $e^\pm$  pairs in a strong magnetic field. *Sov. Phys. JETP* **64**, 1173–1179 (1986).
- Hartin, A. Strong field QED in lepton colliders and electron/laser interactions. *Int. J. Mod. Phys. A* **33**, 1830011 (2018).
- Hartin, A. *Second Order QED Processes in an Intense Electromagnetic Field*. Ph.D. thesis, University of London (2006).
- Baier, V. N., Katkov, V. M. & Strakhovenko, V. M. *Electromagnetic Processes at High Energies in Oriented Single Crystals* (World Scientific, 1998).
- Jansen, O., d’Humières, E., Ribeyre, X., Jequier, S. & Tikhonchuk, V. T. Tree code for collision detection of large numbers of particles applied to the Breit-Wheeler process. *J. Comp. Phys.* **355**, 582–596 (2018).
- Wang, T. et al. Power scaling for collimated  $\gamma$ -ray beams generated by structured laser-irradiated targets and its application to two-photon pair production. *Phys. Rev. Appl.* **13**, 054024 (2020).
- Bragin, S. & Piazza, A. D. Electron-positron annihilation into two photons in an intense plane-wave field. *Phys. Rev. D* **102**, 116012 (2020).
- Arefiev, A. V., Cochran, G. E., Schumacher, D. W., Robinson, A. P. L. & Chen, G. Temporal resolution criterion for correctly simulating relativistic electron motion in a high-intensity laser field. *Phys. Plasmas* **22**, 013103 (2015).
- Gordon, D. & Hafizi, B. Special unitary particle pusher for extreme fields. *Comput. Phys. Commun.* **258**, 107628 (2021).
- Tangtartharakul, K., Chen, G. & Arefiev, A. Particle integrator for particle-in-cell simulations of ultra-high intensity laser-plasma interactions. *J. Comput. Phys.* **434**, 110233 (2021).
- Bethe, H. & Heitler, W. On the stopping of fast particles and on the creation of positive electrons. *Proc. R. Soc. Lond. A* **146**, 83–112 (1934).
- Motz, J. W., Olsen, H. A. & Koch, H. W. Pair production by photons. *Rev. Mod. Phys.* **41**, 581–639 (1969).

## Acknowledgements

This research was supported by AFOSR (Grant No. FA9550-17-1-0382). Simulations were performed with EPOCH (developed under UK EPSRC Grants EP/G054950/1, EP/G056803/1, EP/G055165/1, and EP/M022463/1) using high performance computing resources provided by TACC.

## Author contributions

Y.H. performed the PIC simulations and developed the algorithm to calculate the yield of linear Breit-Wheeler pairs. A.V.A., T.G.B., and T.T. conceived the original idea. All authors contributed to writing and reviewing the manuscript.

## Competing interests

The authors declare no competing interests.



**Additional information**

**Supplementary information** The online version contains supplementary material available at <https://doi.org/10.1038/s42005-021-00636-x>.

**Correspondence** and requests for materials should be addressed to A.V.A.

**Peer review information** *Communications Physics* thanks the anonymous reviewers for their contribution to the peer review of this work.

**Reprints and permission information** is available at <http://www.nature.com/reprints>

**Publisher's note** Springer Nature remains neutral with regard to jurisdictional claims in published maps and institutional affiliations.



**Open Access** This article is licensed under a Creative Commons Attribution 4.0 International License, which permits use, sharing, adaptation, distribution and reproduction in any medium or format, as long as you give appropriate credit to the original author(s) and the source, provide a link to the Creative Commons license, and indicate if changes were made. The images or other third party material in this article are included in the article's Creative Commons license, unless indicated otherwise in a credit line to the material. If material is not included in the article's Creative Commons license and your intended use is not permitted by statutory regulation or exceeds the permitted use, you will need to obtain permission directly from the copyright holder. To view a copy of this license, visit <http://creativecommons.org/licenses/by/4.0/>.

© The Author(s) 2021